AIAA SciTech Forum
4-8 January 2016, San Diego, California, USA
54th AIAA Aerospace Sciences Meeting

Comparison of Drag Prediction Using RANS models and DDES for the DLR-F6 Configuration Using High Order Schemes

Jiaye Gan *
Dept. of Mechanical and Aerospace Engineering, University of Miami
Coral Gables, Florida 33124, USA

Yiqing Shen†
LHD, Institute of Mechanics, Chinese Academy of Sciences,
100190, Beijing, China

Gecheng Zha‡
Dept. of Mechanical and Aerospace Engineering, University of Miami
Coral Gables, Florida 33124, USA

Abstract

This paper compares the accuracy and robustness of steady state RANS, unsteady RANS, and DDES turbulence models with high order schemes for predicting the drag of the DLR-F6 configuration. The implicit time marching method with unfactored Gauss-Seidel line relaxation is used with a 5th order WENO finite difference scheme for Navier-Stokes equations. The viscous terms are discretized using a 4th order conservative central differencing. The effect of grid size on the accuracy of drag prediction by using the different turbulent models are conducted on the coarse, medium and fine mesh models at the same angle of attack. The coarse mesh has about 10 drag counts deviation from the experiment, the medium mesh has 28 counts, and the fine mesh has about 15 counts difference. The RANS method achieves almost the same results as URANS and DDES at angle of attack of 0.49°. The DDES have the least deviation from the experimental drag result and the closest pressure distribution to the experiment in the trailing edge separation zone. However, since the DDES uses the same mesh as the RANS model in this paper, the DDES results should not be considered as conclusive.

1 Introduction

The AIAA CFD Drag Prediction Workshop (DPW) [1, 2, 3, 4, 5] has provided a forum to assess state-of-the-art computational fluid dynamics(CFD) as practical aerodynamic tool for the prediction of forces and moments on industry-relevant aircraft geometry, focusing on drag prediction. In particular, the two configurations, DLR-F6 wing-body and DLR-F6 wing-body-nacelle-pylon, provided at the second AIAA CFD DPW are usually used as the representative complex transonic flows to test the accuracy and performance of CFD codes.

Turbulence modeling is critical for drag prediction, in particular for surface friction drag. The commonly used models today are still the Reynolds averaged Navier-Stokes(RANS) models, which is in general

* Ph.D. student, AIAA Member
† Ph.D., AIAA Member
‡ AIAA Associate Fellow, gzha@miami.edu

considered as inaccurate for predicting the flow with large separations. RANS model treat large eddy structures as isotropic and are not consistent with the physics. However, RANS models have their advantage of CPU efficiency and can handle many engineering problems with calibrated models. The recent Detached Eddy Simulation (DES) of Spalart[6] and Delayed DES[7] are more and more used for their better capability to treat separated flows. Since the configuration of DLR-F6 wing-body has flow separation in the wing-body conjunction, the DDES model is also used for comparison with the RANS and unsteady RANS(URANS) in this paper for the drag prediction. The same mesh provided by the workshop are used for the RANS model and DDES model, even though the mesh is generated for RANS models only. In other words, the DDES conducted in this paper should be treated as a rough reference instead of being conclusive. A more rigorous mesh refinement for DDES will be conducted as the next step. In addition to turbulence modeling, accurate resolving shock waves and viscous terms with minimal numerical dissipation is also crucial for skin friction prediction. The high order numerical schemes, in general higher than 2nd order, are preferred for this purpose. For numerical simulation of complicated transonic flow fields, it is required that the numerical schemes have the ability of shock capturing and fine-scale feature resolution. Due to the capability of capturing shock waves and high order accuracy in smooth regions, the WENO (weighted essentially non-oscillatory) schemes are a desirable option for transonic flows with shock waves.

The WENO scheme concept was first proposed by Liu et al[8] and then improved by Jiang and Shu[9]. Henrick et al[10] pointed out that the original smoothness indicators of Jiang and Shu fail to improving the accuracy order of WENO scheme at a critical point, where the first derivative is zero. A mapping function is proposed by Henrick et al[10] to obtain the optimal order near critical points. Borges et al[11] devised a new set of WENO weights that satisfies the necessary and sufficient conditions for fifth-order convergence proposed by Henrick et al[10] and enhances the accuracy at critical points. Wang and Chen [12] proposed optimized WENO schemes for linear waves with discontinuity. Shen and Zha[13] found that most of all the WENO schemes do not obtain the optimal accuracy near discontinuities. They introduced fourth-order fluxes to overcome this drawback. For transonic flows, Shen et al [14] suggested to use an optimized ε in the smoothness estimators to achieve optimal weight in smooth regions in order to minimize dissipation. A class of higher than 5th order weighted essentially non-oscillatory schemes are designed by Balsara and Shu in [15]. Martin et al[16] proposed a symmetric WENO method by means of a new candidate stencil, the new schemes are $2r$th-order accurate and symmetric, and less dissipative than Jiang and Shu's scheme.

High-order accuracy requires high order evaluation of both the inviscid and viscous fluxes. In order to obtain a high order formulation for viscous terms with a compact width, Shen and Zha[17, 18] constructed a new set of high order conservative schemes, in which all points involved in the interface flux(viscous term) calculation are used to approximate the first derivative in the stress tensor. The new schemes can reach the maximal accuracy by using the least points. This is important to maintain the compactness of the overall discretization schemes and facilitate boundary condition treatment.

The purpose of this paper is to compares the accuracy and robustness of RANS, URANS and DDES turbulence models with high order schemes for predicting the lift and drag of the DLR-F6 configuration. The implicit time marching method with unfactored Gauss-Seidel line relaxation is used with the 5th order WENO finite difference scheme described in[14] for solving the Navier-Stokes equations. The viscous terms are discretized using the 4th order conservative central differencing suggested by Shen and Zha[17]. In this paper, several cases are calculated and the numerical results agree well with the experiment.

2 Numerical Algorithm

2.1 Governing Equations

The governing equations for the flow field computation are the spatially filtered 3D time accurate compressible Navier-Stokes equations in generalized coordinates(ξ, η, ζ) and can be expressed as the following

conservative form:

$$\frac{\partial \mathbf{Q}}{\partial t}+\frac{\partial \mathbf{E}}{\partial \xi}+\frac{\partial \mathbf{F}}{\partial \eta}+\frac{\partial \mathbf{G}}{\partial \zeta}=\frac{1}{Re}\left(\frac{\partial \mathbf{R}}{\partial \xi}+\frac{\partial \mathbf{S}}{\partial \eta}+\frac{\partial \mathbf{T}}{\partial \zeta}\right)+\mathbf{D} \tag{1}$$

where Re is the Reynolds number. Delayed detached eddy simulation(DDES) turbulence model introduced by Sparlat et al.[7] is used to close the system of equations. The equations are nondimenisonalized based on the blade chord length L_∞, upstream characteristic density ρ_∞ and velocity U_∞.

The conservative variable vector $\mathbf{Q}$, the inviscid flux vectors $\mathbf{E}$, $\mathbf{F}$, $\mathbf{G}$, the viscous fluxes $\mathbf{R}$, $\mathbf{S}$, $\mathbf{T}$ and the source term vector $\mathbf{D}$ are expressed as

$$\mathbf{Q}=\frac{1}{J}\begin{pmatrix}\bar{\rho}\\ \bar{\rho}\tilde{u}\\ \bar{\rho}\tilde{v}\\ \bar{\rho}\tilde{w}\\ \bar{\rho}\tilde{e}\\ \bar{\rho}\tilde{\nu}\end{pmatrix},\mathbf{E}=\begin{pmatrix}\bar{\rho}U\\ \bar{\rho}\tilde{u}U+l_x\bar{p}\\ \bar{\rho}\tilde{v}U+l_y\bar{p}\\ \bar{\rho}\tilde{w}U+l_z\bar{p}\\ \left(\bar{\rho}\tilde{e}+\bar{p}\right)U-l_t\bar{p}\\ \bar{\rho}\tilde{\nu}U\end{pmatrix} \tag{2}$$

$$\mathbf{F}=\begin{pmatrix}\bar{\rho}V\\ \bar{\rho}\tilde{u}V+m_x\bar{p}\\ \bar{\rho}\tilde{v}V+m_y\bar{p}\\ \bar{\rho}\tilde{w}V+m_z\bar{p}\\ \left(\bar{\rho}\tilde{e}+\bar{p}\right)V-m_t\bar{p}\\ \bar{\rho}\tilde{\nu}V\end{pmatrix} \tag{3}$$

$$\mathbf{G}=\begin{pmatrix}\bar{\rho}W\\ \bar{\rho}\tilde{u}W+n_x\bar{p}\\ \bar{\rho}\tilde{v}W+n_y\bar{p}\\ \bar{\rho}\tilde{w}W+n_z\bar{p}\\ \left(\bar{\rho}\tilde{e}+\bar{p}\right)W-n_t\bar{p}\\ \bar{\rho}\tilde{\nu}W\end{pmatrix} \tag{4}$$

$$\mathbf{R}=\begin{pmatrix}0\\ l_k\bar{\tau}_{xk}\\ l_k\bar{\tau}_{yk}\\ l_k\bar{\tau}_{zk}\\ l_k\left(\tilde{u}_i\bar{\tau}_{ki}-\bar{q}_k\right)\\ \frac{\bar{\rho}}{\sigma}\left(\nu+\tilde{\nu}\right)\left(\mathbf{l}\bullet\nabla\tilde{\nu}\right)\end{pmatrix} \tag{5}$$

$$\mathbf{S}=\begin{pmatrix}0\\ m_k\bar{\tau}u_{xk}\\ m_k\bar{\tau}_{yk}\\ m_k\bar{\tau}u_{zk}\\ m_k\left(\tilde{u}_i\bar{\tau}_{ki}-\bar{q}_k\right)\\ \frac{\bar{\rho}}{\sigma}\left(\nu+\tilde{\nu}\right)\left(\mathbf{m}\bullet\nabla\tilde{\nu}\right)\end{pmatrix} \tag{6}$$

$$\mathbf{T}=\begin{pmatrix}0\\ n_k\bar{\tau}_{xk}\\ n_k\bar{\tau}_{yk}\\ n_k\bar{\tau}_{zk}\\ n_k\left(\tilde{u}_i\bar{\tau}_{ki}-\bar{q}_k\right)\\ \frac{\bar{\rho}}{\sigma}\left(\nu+\tilde{\nu}\right)\left(\mathbf{n}\bullet\nabla\tilde{\nu}\right)\end{pmatrix} \tag{7}$$

$$\mathbf{D} = \frac{1}{J}\begin{pmatrix} 0 \\ 0 \\ 0 \\ 0 \\ 0 \\ S_\nu \end{pmatrix} \tag{8}$$

where ρ is the density, p is the static pressure, and e is the total energy per unit mass. The overbar denotes a regular filtered variable, and the tilde is used to denote the Favre filtered variable. U, V and W are the contravariant velocities in ξ, η, ζ directions, and defined as follows.

$$U = l_t + \mathbf{l} \bullet \mathbf{V} = l_t + l_x\tilde{u} + l_y\tilde{v} + l_z\tilde{w} \tag{9}$$

$$V = m_t + \mathbf{m} \bullet \mathbf{V} = m_t + m_x\tilde{u} + m_y\tilde{v} + m_z\tilde{w} \tag{10}$$

$$W = n_t + \mathbf{n} \bullet \mathbf{V} = n_t + n_x\tilde{u} + n_y\tilde{v} + n_z\tilde{w} \tag{11}$$

where l_t, m_t and n_t are the components of the interface contravariant velocity of the control volume in ξ, η and ζ directions respectively. $\mathbf{l}$, $\mathbf{m}$ and $\mathbf{n}$ denote the normal vectors located at the centers of ξ, η and ζ interfaces of the control volume with their magnitudes equal to the surface areas and pointing to the directions of increasing ξ, η and ζ. J is the Jacobian of the transformation. The source term S_ν in eq. (8), is given by

$$\begin{gathered} S_\nu = \bar{\rho}C_{b1}\left(1 - f_{t2}\right)\tilde{S}\tilde{\nu} \\ +\tfrac{1}{Re}\left[-\bar{\rho}\left(C_{w1}f_w - \tfrac{C_{b1}}{\kappa^2}f_{t2}\right)\left(\tfrac{\tilde{\nu}}{d}\right)^2\right. \\ \left.+\tfrac{\bar{\rho}}{\sigma}C_{b2}\left(\nabla\tilde{\nu}\right)^2 - \tfrac{1}{\sigma}\left(\tilde{\nu} + \tilde{\nu}\right)\nabla\tilde{\nu} \bullet \nabla\bar{\rho}\right] \\ +Re\left[\bar{\rho}f_{t1}\left(\Delta q\right)^2\right] \end{gathered} \tag{12}$$

where

$$\tilde{\nu} = \nu f_{v1} \qquad \chi = \frac{\tilde{\nu}}{\nu} \tag{13}$$

$$f_{v1} = \frac{\chi^3}{\chi^3 + c_{v1}^3} \qquad f_{v2} = 1 - \frac{\chi}{1 + \chi f_{v1}} \tag{14}$$

$$f_{t1} = C_{t1}g_t exp\left[-C_{t2}\frac{\omega_t^2}{\Delta U^2}\left(d^2 + g_t^2 d_t^2\right)\right] \tag{15}$$

$$f_{t2} = C_{t3}exp\left(-C_{t4}\chi^2\right) \qquad f_w = g(\frac{1 + c_{w3}^6}{g^6 + c_{w3}^6})^{1/6} \tag{16}$$

$$g = r + c_{w2}(r^6 - r) \qquad g_t = min\left(0.1, \frac{\Delta q}{\omega_t \Delta x_t}\right) \tag{17}$$

$$\tilde{S} = S + \frac{\tilde{\nu}}{k^2 d^2}f_{v2} \tag{18}$$

$$r = \frac{\tilde{\nu}}{\tilde{S}k^2 d^2} \tag{19}$$

where, ω_t is the wall vorticity at the wall boundary layer trip location, d is the distance to the closest wall, d_t is the distance of the field point to the trip location, Δq is the difference of the velocities between the field point and the trip location, Δx_t is the grid spacing along the wall at the trip location. The values

of the coefficients are: $c_{b1} = 0.1355, c_{b2} = 0.622, \sigma = \frac{2}{3}, c_{w1} = \frac{c_{b1}}{k^2} + (1 + c_{b2})/\sigma, c_{w2} = 0.3, c_{w3} = 2, k = 0.41, c_{v1} = 7.1, c_{t1} = 1.0, c_{t2} = 2.0, c_{t3} = 1.1, c_{t4} = 2.0$.

The shear stress $\bar{\tau}_{ik}$ and total heat flux $\bar{q}_k$ in Cartesian coordinates is given by

$$\bar{\tau}_{ik} = (\tilde{\mu} + \tilde{\mu}_{DES}) \left[\left(\frac{\partial \tilde{u}_i}{\partial x_k} + \frac{\partial \tilde{u}_k}{\partial x_i} \right) - \frac{2}{3} \delta_{ik} \frac{\partial \tilde{u}_j}{\partial x_j} \right] \tag{20}$$

$$\bar{q}_k = - \left(\frac{\tilde{\mu}}{Pr} + \frac{\tilde{\mu}_{DES}}{Pr_t} \right) \frac{\partial \tilde{T}}{\partial x_k} \tag{21}$$

where μ is from Sutherland's law, and $\mu_{DES} (= \bar{\rho} \tilde{\nu} f_{v1})$ is determined by DES model. The above equations are in tensor form, where the subscripts i, k represents the coordinates x, y, z and the Einstein summation convention is used. Eq.(20) and (21) are transformed to the generalized coordinate system in computation.

In DES, a modification of a S-A based RANS model in which the model switches to a subgrid scale formulation in regions for LES calculations. The coefficients c_{t1} and c_{t3} in the S-A model are set to zero and the distance to the nearest wall, d, is replaced by $\tilde{d}$ as

$$\tilde{d} = min(d, C_{DES} \Delta) \tag{22}$$

where Δ is the largest spacing of the grid cell in all the directions. Within the boundary layer close to the wall, $\tilde{d} = d$, hence the turbulence is simulated by RANS mode of Spalart-Allmaras[19]. Away from the boundary layer, $\tilde{d} = C_{DES} \Delta$ is most of the cases. When the production and destruction terms of the model are balanced, the length scale $\tilde{d}$ will have a Smagorinsky-like eddy viscosity and the turbulence is simulated by the LES model. The coefficient $C_{DES} = 0.65$ is used as set in the homogeneous turbulence[20]. The Pr_t may take the value of 0.9 within the boundary layer for RANS mode and 0.5 for LES mode away from the wall surface.

To overcome the modeled stress depletion problem and make the DES limiter independent of grid spacing, the DDES model suggested by Spalart et al.[7] switches the subgrid scale formulation in DES model by redefining the distance to the nearest wall $\tilde{d}$ as

$$\tilde{d} = d - f_d max(0, d - C_{DES} \Delta) \tag{23}$$

where

$$f_d = 1 - tanh([8 r_d]^3) \tag{24}$$

$$r_d = \frac{\nu_t + \nu}{(U_{i,j} U_{i,j})^{0.5} k^2 d^2 R_e} \tag{25}$$

$$U_{i,j} = \frac{\partial u_i}{\partial x_j} \tag{26}$$

$U_{i,j}$ represents the velocity gradient, and k denotes the Karmann constant. Within the boundary layer close to walls, $\tilde{d} = d$, and away from the boundary layer, $\tilde{d} = d - f_d(d - C_{DES} \Delta)$ is most of the case. This mechanism enables DDES to behave as a RANS model in the near-wall region, and LES away from walls. This modification in $\tilde{d}$ reduces the grey transition area between RANS and LES.

The equation of state as a constitutive equation relating density to pressure and temperature is defined as:

$$\bar{\rho} \tilde{e} = \frac{\bar{p}}{(\gamma - 1)} + \frac{1}{2} \bar{\rho} (\tilde{u}^2 + \tilde{v}^2 + \tilde{w}^2) \tag{27}$$

where γ is the ratio of specific heats. For simplicity, all the bar and tilde in above equations will be dropped in the rest of this paper.

2.2 The Low Diffusion E-CUSP Scheme for Inviscid Flux

The Low Diffusion E-CUSP(LDE) Scheme[21, 22] is used to evaluate the inviscid fluxes. The basic idea of the LDE scheme is to split the inviscid flux into the convective flux E^c and the pressure flux E^p based on the upwind characteristics. With an extra equation from the DDES model, the splitting is basically the same as the original scheme for the Euler equation. This is an advantage over the Roe scheme[23], for which the eigenvectors need to be derived when any extra equation is added to the governing equations. In generalized coordinate system, the flux $\mathbf{E}$ can be split as the following:

$$\mathbf{E}' = E^c + E^p = \begin{pmatrix} \rho U \\ \rho u U \\ \rho v U \\ \rho w U \\ \rho e U \\ \rho \tilde{\nu} U \end{pmatrix} + \begin{pmatrix} 0 \\ l_x p \\ l_y p \\ l_z p \\ p\overline{U} \\ 0 \end{pmatrix} \tag{28}$$

where, U is the contravariant velocity in ξ direction and is defined as the following:

$$U = l_t + l_x u + l_y v + l_z w \tag{29}$$

$\overline{U}$ is defined as:

$$\overline{U} = l_x u + l_y v + l_z w \tag{30}$$

The convective term, E^c is evaluated by

$$E^c = \rho U \begin{pmatrix} 1 \\ u \\ v \\ w \\ e \\ \tilde{\nu} \end{pmatrix} = \rho U f^c, \; f^c = \begin{pmatrix} 1 \\ u \\ v \\ w \\ e \\ \tilde{\nu} \end{pmatrix} \tag{31}$$

let

$$C = c\left(l_x^2 + l_y^2 + l_z^2\right)^{\frac{1}{2}} \tag{32}$$

where $c = \sqrt{\gamma RT}$ is the speed of sound.

Then the convective flux at interface $i + \frac{1}{2}$ is evaluated as:

$$E^c_{i+\frac{1}{2}} = C_{\frac{1}{2}} \left[\rho_L C^+ f^c_L + \rho_R C^- f^c_R\right] \tag{33}$$

where, the subscripts L and R represent the left and right hand sides of the interface. The Mach number splitting of Edwards[24] is borrowed to determine c^+ and c^- as the following:

$$C_{\frac{1}{2}} = \frac{1}{2}\left(C_L + C_R\right) \tag{34}$$

$$C^+ = \alpha^+_L \left(1 + \beta_L\right) M_L - \beta_L M^+_L - M^+_{\frac{1}{2}} \tag{35}$$

$$C^- = \alpha_R^- (1 + \beta_R) M_R - \beta_R M_R^- + M_{\frac{1}{2}}^- \tag{36}$$

$$M_L = \frac{U_L}{C_{\frac{1}{2}}},\ M_R = \frac{U_R}{C_{\frac{1}{2}}} \tag{37}$$

$$\alpha_{L,R} = \tfrac{1}{2} \left[1 \pm sign\left(M_{L,R}\right)\right] \tag{38}$$

$$\beta_{L,R} = -max\left[0, 1 - int\left(|M_{L,R}|\right)\right] \tag{39}$$

$$M_{\frac{1}{2}}^+ = M_{\frac{1}{2}} \frac{C_R + C_L \Phi}{C_R + C_L},\ M_{\frac{1}{2}}^- = M_{\frac{1}{2}} \frac{C_L + C_R \Phi^{-1}}{C_R + C_L} \tag{40}$$

$$\Phi = \frac{\left(\rho C^2\right)_R}{\left(\rho C^2\right)_L} \tag{41}$$

$$M_{\frac{1}{2}} = \beta_L \delta^+ M_L^- - \beta_R \delta^- M_R^+ \tag{42}$$

$$M_{L,R}^{\pm} = \pm \tfrac{1}{4} \left(M_{L,R} \pm 1\right)^2 \tag{43}$$

$$\delta^{\pm} = \tfrac{1}{2} \left\{1 \pm sign\left[\tfrac{1}{2}\left(M_L + M_R\right)\right]\right\} \tag{44}$$

The pressure flux, E^p is evaluated as the following

$$E_{i+\frac{1}{2}}^p = \begin{pmatrix} 0 \\ \mathcal{P}^+ p\, l_x \\ \mathcal{P}^+ p\, l_y \\ \mathcal{P}^+ p\, l_z \\ \frac{1}{2} p \left[\overline{U} + \overline{C}_{\frac{1}{2}}\right] \\ 0 \end{pmatrix}_L + \begin{pmatrix} 0 \\ \mathcal{P}^- p\, l_x \\ \mathcal{P}^- p\, l_y \\ \mathcal{P}^- p\, l_z \\ \frac{1}{2} p \left[\overline{U} - \overline{C}_{\frac{1}{2}}\right] \\ 0 \end{pmatrix}_R \tag{45}$$

The contravariant speed of sound $\overline{C}$ in the pressure vector is consistent with $\overline{U}$. It is computed based on C as the following,

$$\overline{C} = C - l_t \tag{46}$$

The use of $\overline{U}$ and $\overline{C}$ instead of U and C in the pressure vector is to take into account of the grid speed so that the flux will transit from subsonic to supersonic smoothly. When the grid is stationary, $l_t = 0$, $\overline{C} = C$, $\overline{U} = U$.

The pressure splitting coefficient is:

$$\mathcal{P}_{L,R}^{\pm} = \frac{1}{4} \left(M_{L,R} \pm 1\right)^2 \left(2 \mp M_L\right) \tag{47}$$

The LDE scheme can capture crisp shock profile and exact contact surface discontinuities as accurately as the Roe scheme[22]. However, it is simpler and more CPU efficient than the Roe scheme due to no matrix operation. In the reference[25], the LDE scheme is shown to be more efficient than the Roe scheme when the S-A one equation turbulence model is coupled.

2.3 The WENO Scheme[9]

The WENO scheme is used to evaluate the conservative variables U^L and U^R. The WENO scheme for a variable u^L can be written as:

$$u^L_{i+1/2} = \sum_{k=0}^{r} \omega_k q_k \tag{48}$$

where $\omega_k (k = 0, \cdots, r)$ are the weights, and the $q_k (k = 0, \cdots, r)$ are the rth order accuracy reconstruction of the variables in three different stencils.

$$\omega_k = \frac{\alpha_k}{\alpha_0 + \cdots + \alpha_{r-1}}, \tag{49}$$

where

$$\alpha_k = \frac{C_k}{(\varepsilon + IS_k)^p}, \quad k = 0, 1, 2 \tag{50}$$

where C_k are the optimal weights with the following values.

The smoothness indicators IS_k suggested by Jiang and Shu[9] are given by

$$IS_k = \sum_{l=1}^{r-1} \Delta x^{2l-1} \int_{x_{i-\frac{1}{2}}}^{x_{i+\frac{1}{2}}} (\frac{d^l}{dx^l} \hat{q}_k(x))^2 dx \tag{51}$$

The ε in Eq.(50) is introduced to avoid the denominator becoming zero. Jiang and Shu's numerical tests indicate that the results are not sensitive to the choice of ε as long as it is in the range of 10^{-5} to 10^{-7}. In their paper[9], ε is taken as 10^{-6}. In [14], Shen et al suggested to use an optimized ε value of 10^{-2} in the smoothness estimators to achieve optimal weight in smooth regions in order to minimize dissipation and improve convergence.

The u^R is constructed symmetrically as u^L about $i + 1/2$.

For the third-order($r = 2$) WENO scheme, there are

$$q_0 = -\frac{1}{2}u_{i-1} + \frac{3}{2}u_i, \quad q_1 = \frac{1}{2}u_i + \frac{1}{2}u_{i+1}$$

and

$$\begin{gathered} C_0 = 1/3, \quad C_1 = 2/3 \\ IS_0 = (u_i - u_{i-1})^2, \quad IS_1 = (u_{i+1} - u_i)^2 \end{gathered} \tag{52}$$

For the fifth-order($r = 3$) WENO scheme, there are

$$\begin{aligned} q_0 &= \frac{1}{3}u_{i-2} - \frac{7}{6}u_{i-1} + \frac{11}{6}u_i \\ q_1 &= -\frac{1}{6}u_{i-1} + \frac{5}{6}u_i + \frac{1}{3}u_{i+1} \\ q_2 &= \frac{1}{3}u_i + \frac{5}{6}u_{i+1} - \frac{1}{6}u_{i+2} \end{aligned}$$

and

$$C_0 = 0.1, \quad C_1 = 0.6, \quad C_2 = 0.3$$

and IS_k are

$$\begin{aligned} IS_0 &= \tfrac{13}{12}(u_{i-2} - 2u_{i-1} + u_i)^2 + \tfrac{1}{4}(u_{i-2} - 4u_{i-1} + 3u_i)^2 \\ IS_1 &= \tfrac{13}{12}(u_{i-1} - 2u_i + u_{i+1})^2 + \tfrac{1}{4}(u_{i-1} - u_{i+1})^2 \\ IS_2 &= \tfrac{13}{12}(u_i - 2u_{i+1} + u_{i+2})^2 + \tfrac{1}{4}(3u_i - 4u_{i+1} + u_{i+2})^2 \end{aligned} \tag{53}$$

2.4 The 4th-Order Schemes for Viscous Terms[17]

A set of fully conservative 4th-order accurate finite central differencing schemes using the same stencil width of the WENO scheme for the viscous terms is used in this paper. The scheme for the viscous derivative term $\frac{\partial R}{\partial \xi}$ in Navier-Stokes equations Eq.(1) can be written as the following,

$$\frac{\partial R}{\partial \xi}|_i = \frac{\tilde{R}_{i+1/2} - \tilde{R}_{i-1/2}}{\Delta \xi} \tag{54}$$

To obtain 4th order accuracy, $\tilde{R}$ needs to be reconstructed as

$$\tilde{R}_{i-1/2} = \sum_{I=i-3/2}^{i+1/2} \alpha_I R_I \tag{55}$$

where

$$\begin{aligned} \alpha_{i-3/2} = -\frac{1}{24},\ \alpha_{i-1/2} = \frac{26}{24},\ \alpha_{i+3/2} = -\frac{1}{24} \\ R_{i-1/2} = \left[(\xi_x \tau_{xx}) + (\eta_y \tau_{xy}) + (\zeta_z \tau_{xz})\right]_{i-1/2} \\ \begin{aligned} (\tau_{xx}) = \ & \mu\{\tfrac{4}{3}\left[(\xi_x \tfrac{\partial u}{\partial \xi}) + (\eta_x \tfrac{\partial u}{\partial \eta}) + (\zeta_x \tfrac{\partial u}{\partial \zeta})\right] \\ & -\tfrac{2}{3}[(\xi_y \tfrac{\partial v}{\partial \xi}) + (\eta_y \tfrac{\partial v}{\partial \eta}) + (\zeta_y \tfrac{\partial v}{\partial \zeta}) \\ & (\xi_z \tfrac{\partial w}{\partial \xi}) + (\eta_z \tfrac{\partial w}{\partial \eta}) + (\zeta_z \tfrac{\partial w}{\partial \zeta})]\} \end{aligned} \end{aligned} \tag{56}$$

If R_I in Eq.(55) can be approximated with the accuracy order not lower than 4th order, the Taylor expansion analysis of (54) and (55) will give the following relation[17],

$$\frac{1}{\Delta \xi}(\tilde{R}_{i+1/2} - \tilde{R}_{i-1/2}) = R^{'}(\xi_i) + O(\Delta \xi^4) \tag{57}$$

i.e. the 4th order accuracy is achieved.

In order to achieve the highest order accuracy of R_I with $I = i-3/2, i-1/2, i+1/2$, the approximation of each component in Eq. (55) using all the involved points of the WENO stencil is given below:

$$\mu_I = \sum_{l=m}^{n} C_l^I \mu_{i+l}, \tag{58}$$

$$\frac{\partial u}{\partial \xi}|_I = \frac{1}{\Delta \xi} \sum_{l=r}^{s} D_l^I u_{i+l}, \tag{59}$$

$$\frac{\partial u}{\partial \eta}|_I = \sum_{l=m}^{n} C_l^I \frac{\partial u}{\partial \eta}|_{i+l,j} \tag{60}$$

where

$$\frac{\partial u}{\partial \eta}|_{i,j} = \frac{1}{\Delta \eta} \sum_{l=p}^{q} C_l^c u_{i,j+l}, \tag{61}$$

By choosing different ranges for $(m,n),(r,s),(p,q)$ and different coefficients C_l^I, D_l^I, C_l^c, one can obtain different order accuracy approximation to the viscous terms. The principle of choosing $(m,n),(r,s),(p,q)$ is to ensure that the approximation of $\frac{\partial R}{\partial \xi}|_i$ in Eq.(54) is a central differencing. For example, in this paper, $(m,n) = (-2,1),(r,s) = (-3,2), and\ (p,q) = (-2,2)$ are used, and they give[17],

$$\mu_I = \sum_{l=m}^{n} C_l^I \mu_{i+l} + O(\Delta \xi^4), \tag{62}$$

$$\frac{\partial u}{\partial \xi}|_I = \frac{1}{\Delta \xi} \sum_{l=r}^{s} D_l^I u_{i+l} + O(\Delta \xi^5), \tag{63}$$

$$\frac{\partial u}{\partial \eta}|_I = \sum_{l=m}^{n} C_l^I \frac{\partial u}{\partial \eta}|_{i+l,j} + O(\Delta \xi^4, \Delta \eta^4), \tag{64}$$

where

$$\frac{\partial u}{\partial \eta}|_{i,j} = \frac{1}{\Delta \eta} \sum_{l=p}^{q} C_l^c u_{i,j+l} + O(\Delta \eta^4) \tag{65}$$

the coefficients C_l^I, D_l^I, C_l^c can be obtained by Taylor's series expansion and are given in Tables 1-3.

Table 1: The coefficients of C_l^I

I	C_{-2}^I	C_{-1}^I	C_0^I	C_1^I
$i-3/2$	5/16	15/16	-5/16	1/16
$i-1/2$	-1/16	9/16	9/16	-1/16
$i+1/2$	1/16	-5/16	15/16	5/16

Table 2: The coefficients of D_l^I

I	D_{-3}^I	D_{-2}^I	D_{-1}^I	D_0^I	D_1^I	D_2^I
$i-3/2$	71/1920	-141/128	69/64	1/192	-3/128	3/640
$i-1/2$	-3/640	25/384	-75/64	75/64	-25/384	3/640
$i+1/2$	-3/640	3/128	-1/192	-69/64	141/128	-71/1920

Table 3: The coefficients of C_l^c

C_{-2}^c	C_{-1}^c	C_0^c	C_1^c	C_2^c
1/12	-8/12	0	8/12	-1/12

Shen et al [17] proved that the scheme of Eq. (54) is symmetric with respect to cell i and is of 4th-order accuracy. The symmetry of Eq. (54) satisfies the diffusion property of viscous fluxes.

2.5 Time Marching Scheme

The time dependent governing equation (1) is solved using dual time stepping method suggested by Jameson[26]. A pseudo temporal term $\frac{\partial Q}{\partial \tau}$ is added to the governing Eq. (1). This term vanishes at the end of each physical time step, and has no influence on the accuracy of the solution. An implicit pseudo time marching scheme using Gauss-Seidel line relaxation is employed to achieve high convergence rate instead of using the explicit scheme[27]. The pseudo temporal term is discretized with first order Euler scheme. Let m stand for the iteration index within a physical time step, the semi-discretized governing equation can be expressed as

$$\begin{aligned} &\left[\left(\tfrac{1}{\Delta\tau} + \tfrac{1.5}{\Delta t}\right) I - \left(\tfrac{\partial R}{\partial \mathbf{Q}}\right)^{n+1,m}\right] \delta \mathbf{Q^{n+1,m+1}} \\ &\quad = R^{n+1,m} - \tfrac{\mathbf{3Q^{n+1,m} - 4Q^n + Q^{n-1}}}{2\Delta t} \end{aligned} \tag{66}$$

where $\Delta\tau$ is the pseudo time step, and R is the net flux of the Navier-Stokes equations.

3 Results and Discussion

In this paper, the DLR-F6 wing-body configuration as shown in Fig. 1, which is used by the second AIAA Drag Prediction Workshop, is calculated. The Mach number is 0.75, Reynolds number based on the mean aerodynamic chord is 3.0×10^6. The total pressure and total temperature are given at computational domain inlet as the boundary conditions. The static pressure at the outlet of computational domain is to make the inlet Mach number matching the experimental value. In the far field, zero gradient boundary condition is used. The unsteady DDES calculation reaches the stable solution at about 250 characteristic time. The solution residuals are reduced at least 2 orders of magnitude within each physical time step and the aerodynamic coefficients vary less than 0.1% over the last 100 time steps. The aerodynamic coefficients were the determining factor in convergence in all cases.

3.1 Grid convergence study

The drag prediction workshop had provided a series of grids that include 1-to-1 connected multiblock grid, structured overlap grid, and unstructured grid. The 1-to-1 point matched grid from ICEM is used as a baseline mesh for computation in this paper. Because the mesh topologies near the wing tip from ICEM software are very complex and the mesh size of each block is varied distinctly, computational grids are regenerated to have simpler mesh-topologies and better load balance for parallel computation. The overall topology of the new mesh employs a O-type topology as shown in Fig. 2. The computational domain models only half of the configuration and symmetry boundary conditions are applied to the symmetrical plane. In the new mesh, the first layer of blocks used for the viscous boundary layer computation is kept the same as the supplied mesh. The mesh topologies at the nose, wing tip and tail of the fuselage are changed to the O-type topology, as shown in Fig. 3. The length of the first grid cell in surface normal direction is 0.001 mm. This value was found to be sufficient to achieve a value of y^+ about 1. In order to conduct a grid convergence study, three levels of mesh sizes have been generated. The coarse mesh model has a total of 2184140 grid cells, in which the number of grid points in the boundary layer is 29. The medium mesh model has a total of 6364462 grid cells with 41 points in the boundary layer blocks. And there are 49 grid points in first layer of blocks of in the third level of mesh, resulting a total number of 8410092 grid cells.

All the grid models with DDES method were run at AoA=0.49°. The computed results are shown in Table. 4. For comparison, the experimental data is also listed in the same table. In the table, C_L is lift coefficient and C_D is drag coefficient. The C_L comparison between DDES and experiment is given by relative errors. And the C_D comparison is given by relative drag counts, in which 1 count is 0.0001. It can be seen that there is a linear variation in C_L with the mesh refinement, which indicates that the three cases achieve grid convergence for DDES method. However, the grid convergence test of DDES is not achieved in C_D prediction. The C_D from medium mesh shows about 28 drag counts(0.0028) deviated from experiment and has the maximum relative error of 9.559%. Whereas the coarse level grid has the lowest relative errors of 3.347% with about 10 drag counts. Compared with the coarse and medium mesh model, the fine mesh model provides the lowest relative error in C_L prediction and about 15 drag counts in C_D prediction.

Table 4: Lift, drag coefficients from DDES at AoA=0.49

Item	C_L	error, %	C_D	ΔC_D
Exp	0.498400	0.000	0.029396	0
Coarse	0.479830	3.726	0.030380	10
Medium	0.482161	3.258	0.032206	28
Fine	0.485735	2.541	0.030941	15

The convergence histories of C_L and C_D are shown in Fig. 4 and Fig. 5 respectively. Results of the three different mesh size are plot. It is seen that the calculation converged after about 100 non-dimensional time. The C_L curve predicted by the DDES method is about the same as URANS. And the C_D value predicted by DDES is a little lower than that of URANS.

Fig. 6 to Fig. 13 are the time averaged coefficient of pressure at different wing sections at AoA=0.49°. Each figure shows the DDES results of the coarse, medium and fine grid models. Overall, the numerical results predicted by using DDES agree very well with the experiments, including the shock wave strength and location along the span. All mesh models show large errors at 0.15 span, where there is a separation at wing-body conjunction. This predicted separation location is consistent with the conclusion of the second drag prediction workshop, which concluded that it was the separated flow regions at wing/body junctures cause large error of predicted results and make it difficult to draw meaningful conclusions. It appears that the separation bubble still affect the present results of DDES. Compared to the coarse mesh model, the medium and fine mesh model provide slightly better Cp results at lower span in the 50% chordwise location. The shock location is well resolved in Fig. 8 and Fig. 9, in particular with the medium and fine mesh. Shock location moves more upstream in the mid-span.

Table. 5 lists the two components of total force coefficients, the pressure force coefficient and the friction force coefficient, predicted by using DDES. In the table, px, py and pz are the force coefficients contributed by pressure in x, y, and z direction respectively. And vx, vy, vz are the force coefficients contributed by the viscous shear stresses in x, y, and z direction respectively. The force in x direction contributes to the drag. The force in z direction contributes to the lift. The force in y direction is the lateral force, which should be zero approximately when the whole configuration is considered. The forces are integrated at time step of 6000, which is different from the time averaged results in Table. 4. The breakdown of the force may help to identify the main source of the errors in lift and drag prediction. It can be seen that the general trends of pressure and viscous drag data are consistent with the total drag in mesh refinement study. The pressure drag is converged based on mesh size. It is the friction drag still varies with the mesh size. The table also shows that the viscous drag contribution is about 82% of the pressure drag, a little smaller but in the same order of magnitude. This also indicates that there is a large room to reduce the total drag by reducing the pressure drag. While the viscous lift contribution to the total lift is negligible compared with the lift generated by pressure.

Table 5: Force components of different mesh at AoA=0.49°

Item	px	py	pz	vx	vy	vz
Coarse	0.016301	4.769143	0.479410	0.014063	-0.000113	-0.000139
Medium	0.017135	4.767384	0.478435	0.015037	-0.000008	-0.000077
Fine	0.017158	4.766717	0.481208	0.013719	-0.000072	-0.000108

The surface pressure contours and streamlines of three level of mesh sizes are shown in Fig. 14. The plots compares the wing/body juncture flow at upper-surface wing trailing edge at AoA=0.49° by using DDES method. The separation bubbles are clearly seen in all three mesh simulations and the predicted separation bubbles are about the same. But the fine mesh resolves more detailed flow structures.

3.2 Effect of turbulence modeling

It is useful to compare the DDES results with the commonly used steady RANS model and unsteady RANS(URANS) model. Both RANS and URANS employ the one-equation Spalart-Allmaras (SA) model. Table. 6 and Table. 7 summarize the results of RANS and URANS at AoA=0.49° respectively. The predicted C_L results of both RANS and URANS show good agreement with experiment. The maximum relative errors are less than 3% in all test cases. Still, the coarse mesh provides better results than medium and fine mesh. It is noted that the drag counts predicted by DDES shown in Table. 4 are less than the

drag deviation of both RANS and URANS, in particular for the coarse and medium mesh.

Table 6: Lift, drag coefficients from RANS at AoA=0.49°

Item	C_L	errors, %	C_D	ΔC_D
Exp	0.498400	0.000	0.029396	0
Coarse	0.489087	1.869	0.030937	15
Medium	0.484887	2.711	0.032552	32
Fine	0.486100	2.468	0.030993	16

Table 7: Lift, drag coefficients from URANS at AoA=0.49°

Item	C_L	errors, %	C_D	ΔC_D
Exp	0.498400	0.000	0.029396	0
Coarse	0.488338	2.019	0.030830	14
Medium	0.482526	3.185	0.032527	31
Fine	0.485611	2.566	0.031167	18

Table. 8 lists the total drag coefficients and their two components, the pressure drag coefficient and the friction drag coefficient of the fine mesh, for all the three turbulence modeling methods. The predicted friction drag counts among the three turbulence models are less than one count for the case at AoA=0.49°. The reason appears to be that they all employ the same turbulence modes within the wall boundary layer. For the predicted pressure drag that is more affected by the flow structures outside of the boundary layer, DDES provides about 2 drag counts less than RANS and URANS. The RANS methods has almost the same px value as that of the URANS method, which indicates that unsteady flow effect is not important for this wing body configuration model.

Table 8: Force components of different turbulence modeling method at AoA=0.49°

Item	px	py	pz	vx	vy	vz
RANS	0.017395	4.766450	0.492607	0.013808	-0.000085	-0.000169
URANS	0.017394	4.766713	0.482234	0.013736	-0.000091	-0.000131
DDES	0.017158	4.766717	0.481208	0.013719	-0.000072	-0.000108

The MUSCL and WENO schemes are implemented in current codes for comparison. The comparisons of different reconstruction schemes are listed in Table. 9. MUSCL3 has the 3rd order accuracy for the inviscid flux without using any limiters. WENO3 and WENO5 are the 3rd and 5th order of WENO schemes respectively. The results are from steady state RANS simulation at AoA=0.49°. It can be seen from the table that the prediction by using the WENO5 scheme has larger errors in C_L than that with the 3rd order schemes. And the WENO5 scheme predicts about 2 drag counts lower than those 3rd order schemes and is closer to the experiment.

Fig. 15 are the coefficient of pressure at three typical wing spans at AoA=0.49°. At 0.15 span, all the turbulence modeling methods captured the separation bubble. The DDES gives the best prediction at the tailing edge separation region, which indicates the advantage as it is designed to have. The pressure predicted by the three methods are almost the same at outer span where there is no flow separation.

Fig. 16 shows the lift and the drag versus different angle of attacks. The C_L predicted by all the methods agree very well with the experiment. The C_L errors of URANS and DDES method become larger at higher positive angle of attack. Regarding the C_D curve, numerical results match the experiment at positive angle of attack and show larger errors at negative AoA with the maximum error less than 25 counts. The DDES model again shows a better agreement between the predicted and measured drag than RANS and URANS model at low AoA about 15 counts.

Table 9: Lift, drag coefficient comparisons at AoA=0.49° by using RANS method

Item	C_L	errors, %	C_D	ΔC_D
Exp	0.498400	0.000	0.029396	0
MUSCL3	0.492437	1.196	0.031203	18
WENO3	0.491657	1.353	0.031180	18
WENO5	0.486100	2.468	0.030993	16

4 Conclusions

This paper compares the accuracy and robustness of DDES, RANS, and URANS turbulence modeling using high order schemes for predicting the lift and drag of the DLR-F6 configuration. The implicit time marching method with unfactored Gauss-Seidel line relaxation is used with a 5th order WENO finite difference scheme for Navier-Stokes equations. The viscous terms are discretized using a 4th order conservative central differencing. The effect of grid density, spatial difference schemes and turbulence modeling methods are studied.

Grid convergence in the prediction of lift coefficients is achieved by using DDES method, but the C_D still has variation of over 10 counts. The C_D from medium mesh shows about 28 drag counts(0.0028) deviated from experiment and has the maximum relative error of 9.559%. Compared with the coarse and medium mesh, the fine mesh model provides the lowest error in C_L prediction and about 15 drag counts in C_D prediction. All meshes show large surface pressure deviation at 0.15 span, which is located at separation region of the wing-body conjunction.

The predicted C_L results of both RANS and URANS show good agreement with experiment. The maximum errors are less than 3% in all test cases. The coarse mesh provides better results than medium and fine mesh. The drag counts deviation rom the experiment predicted by the DDES are less than those of both RANS and URANS. This indicates the advantage of DDES in turbulence modeling.

The predicted friction drag counts difference between the URANS and DDES is less than one count for the case at AoA=0.49°. The reason may be that DDES method employ the same turbulence model as URANS within the wall boundary layer. For the predicted pressure drag, DDES provides about 2 drag counts more accurate than RANS and URANS. The prediction by using the 5th WENO scheme provides lower C_L and drag counts than the 3rd order schemes.

The same mesh provided by the workshop are used for the RANS model and DDES model, even though the mesh is generated for RANS models only. In other words, the DDES conducted in this paper should be treated as a rough reference instead of being conclusive. A more rigorous mesh refinement study for DDES drag prediction will be conducted as the next step.

5 Acknowledgment

The computing resource supports from the Center for Computational Sciences at University of Miami is greatly appreciated.

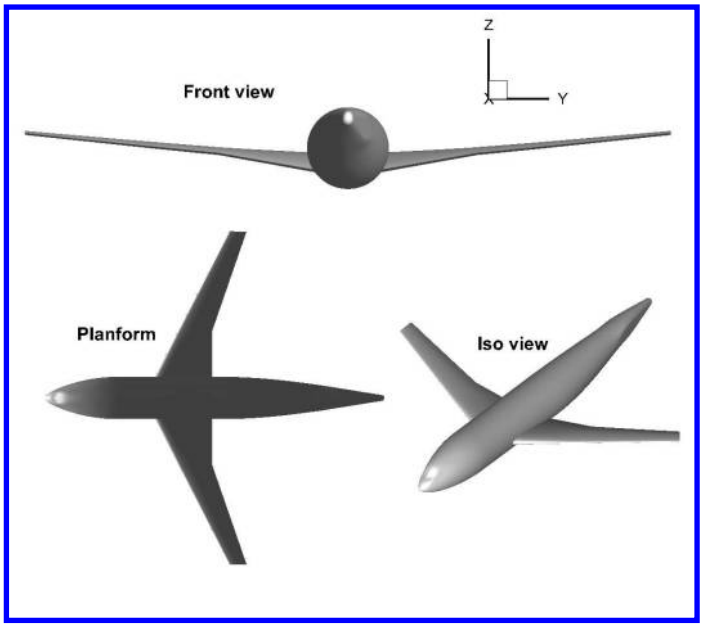

Figure 1: Geometry of wing-body configuration

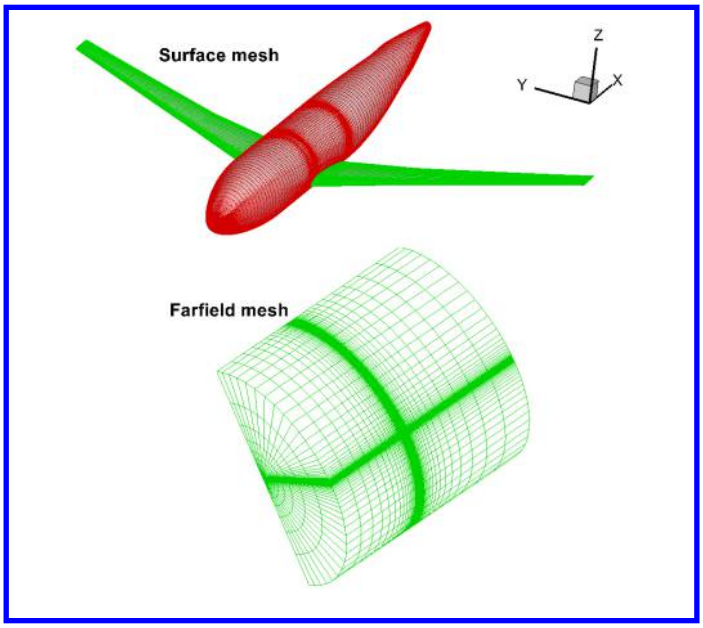

Figure 2: Meshes on wall and far field

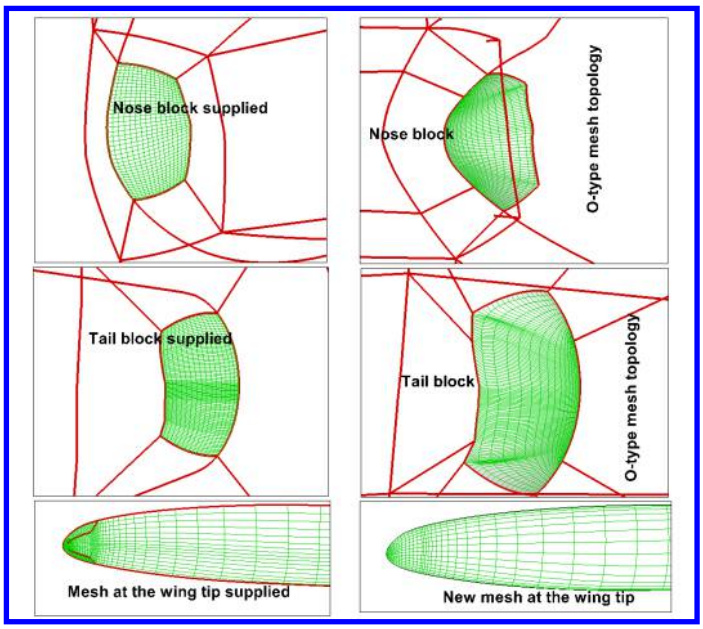

Figure 3: Mesh topology comparison

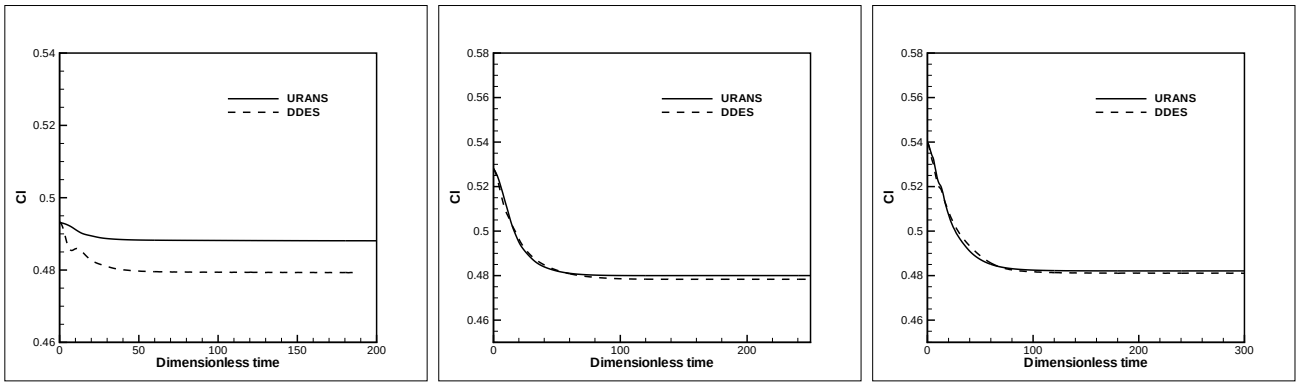

Figure 4: Time history of lift coefficient. Left: Coarse mesh; Middle: Medium mesh; Right: Fine mesh

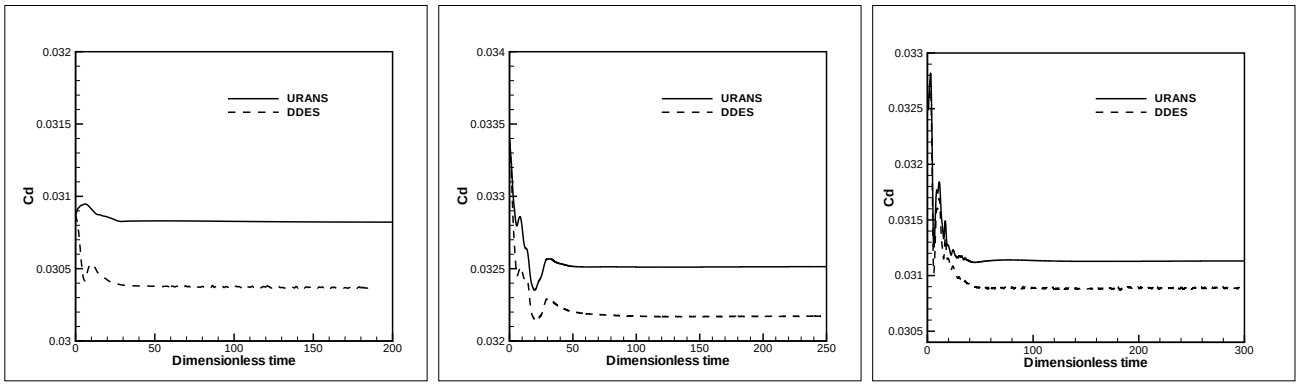

Figure 5: Time history of drag coefficient. Left: Coarse mesh; Middle: Medium mesh; Right: Fine mesh

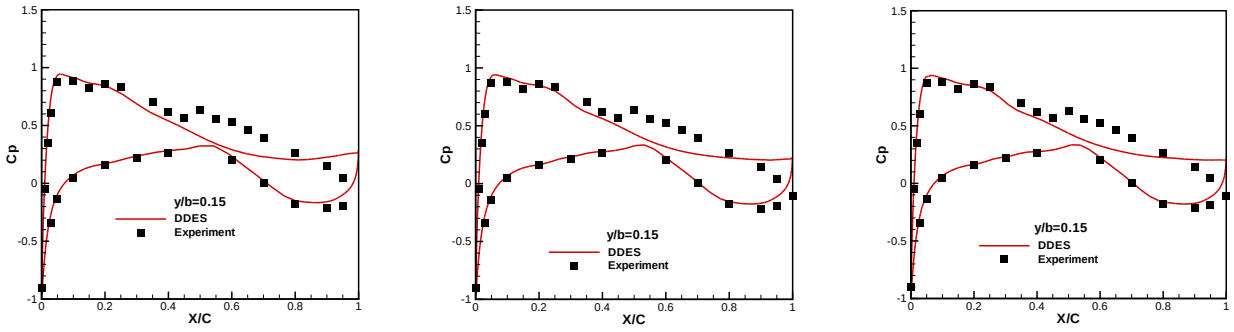

Figure 6: Wing pressure coefficient comparison using DDES at 0.15 semispan. Left: Coarse mesh; Middle: Medium mesh; Right: Fine mesh

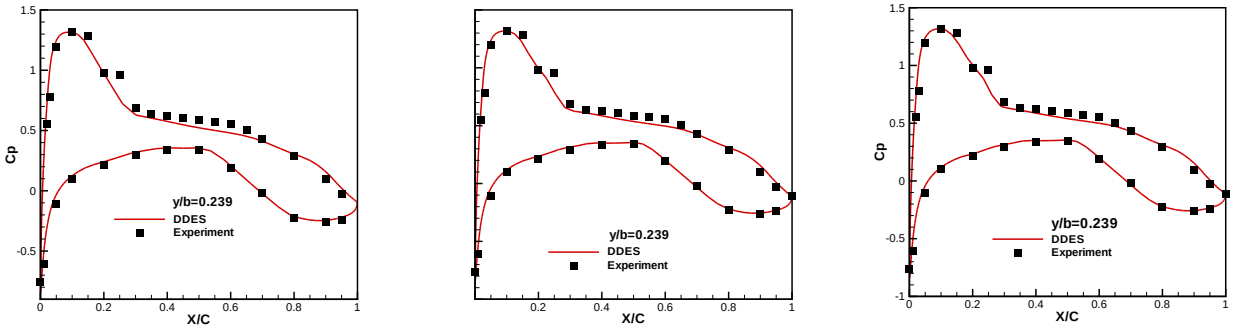

Figure 7: Wing pressure coefficient comparison using DDES at 0.239 semispan. Left: Coarse mesh; Middle: Medium mesh; Right: Fine mesh

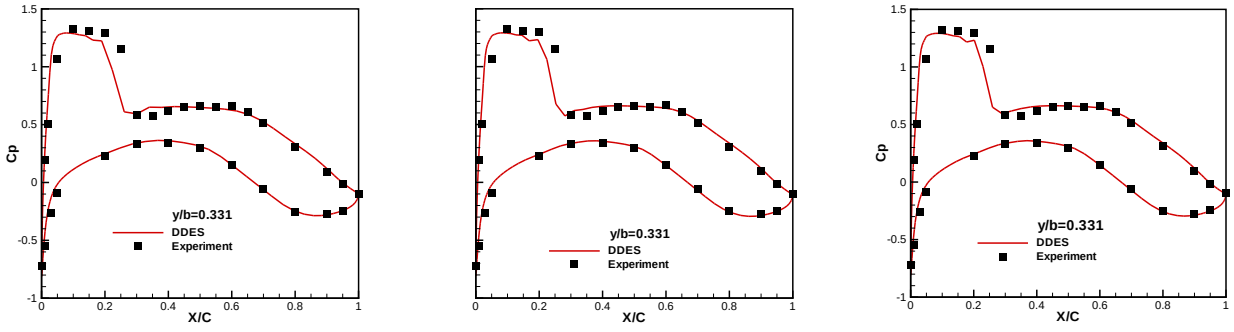

Figure 8: Wing pressure coefficient comparison using DDES at 0.331 semispan. Left: Coarse mesh; Middle: Medium mesh; Right: Fine mesh

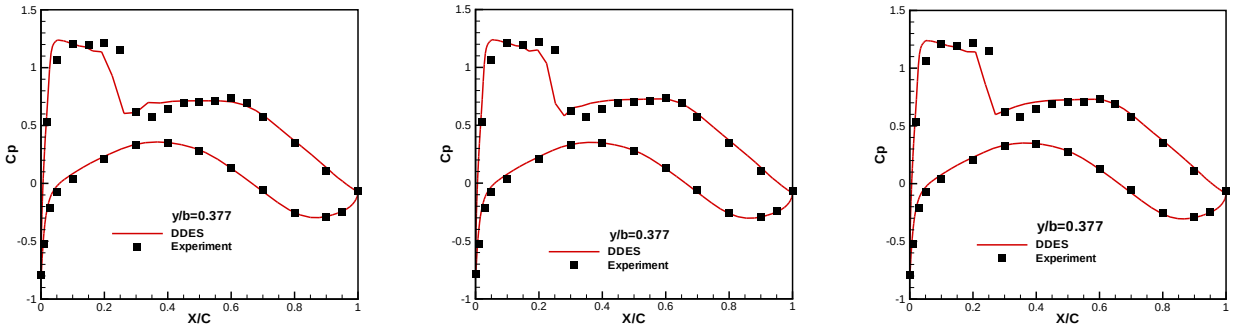

Figure 9: Wing pressure coefficient comparison using DDES at 0.377 semispan. Left: Coarse mesh; Middle: Medium mesh; Right: Fine mesh

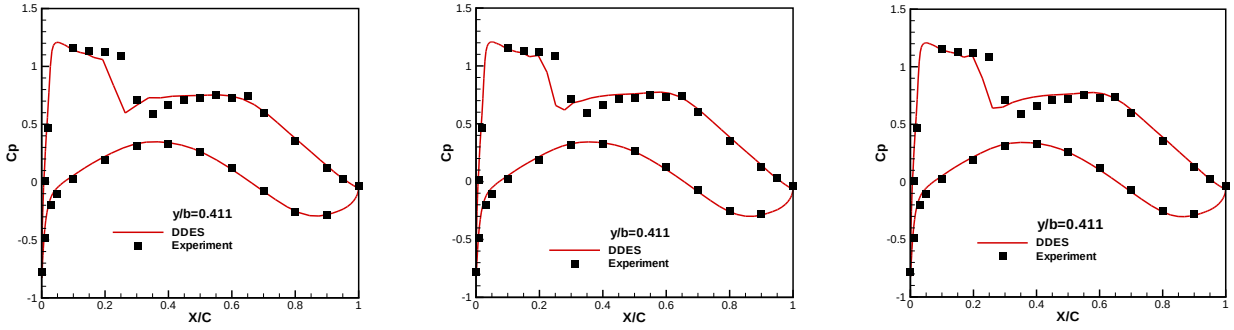

Figure 10: Wing pressure coefficient comparison using DDES at 0.411 semispan. Left: Coarse mesh; Middle: Medium mesh; Right: Fine mesh

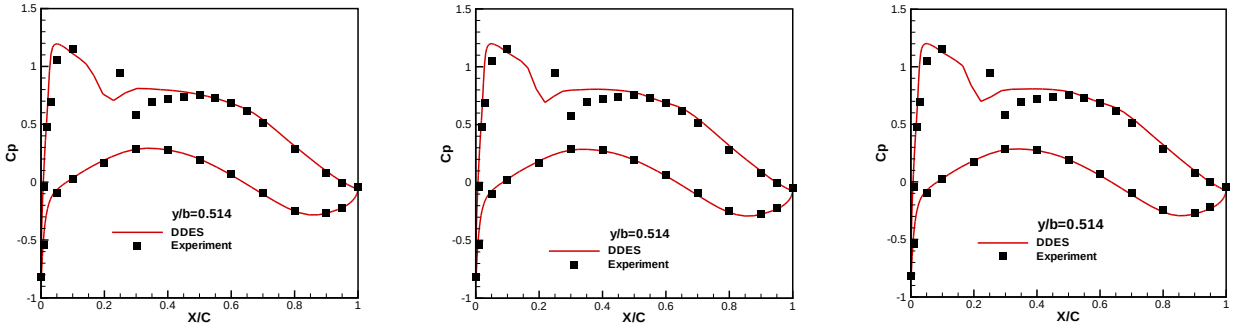

Figure 11: Wing pressure coefficient comparison using DDES at 0.514 semispan. Left: Coarse mesh; Middle: Medium mesh; Right: Fine mesh

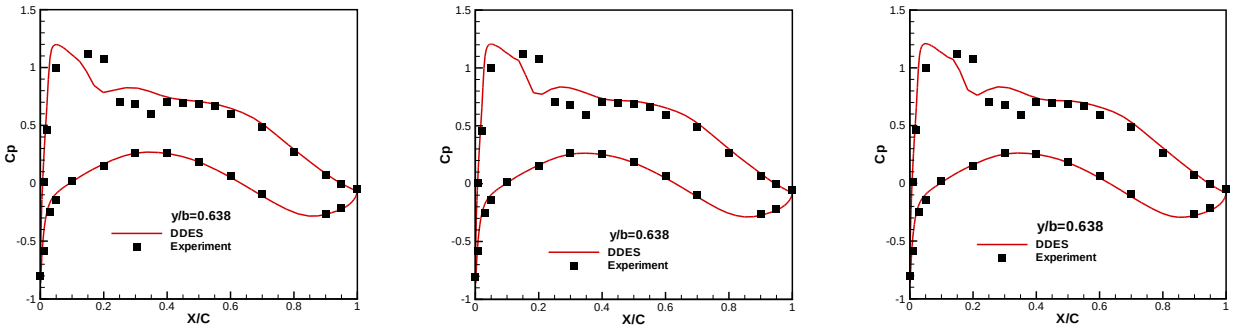

Figure 12: Wing pressure coefficient comparison using DDES at 0.638 semispan. Left: Coarse mesh; Middle: Medium mesh; Right: Fine mesh

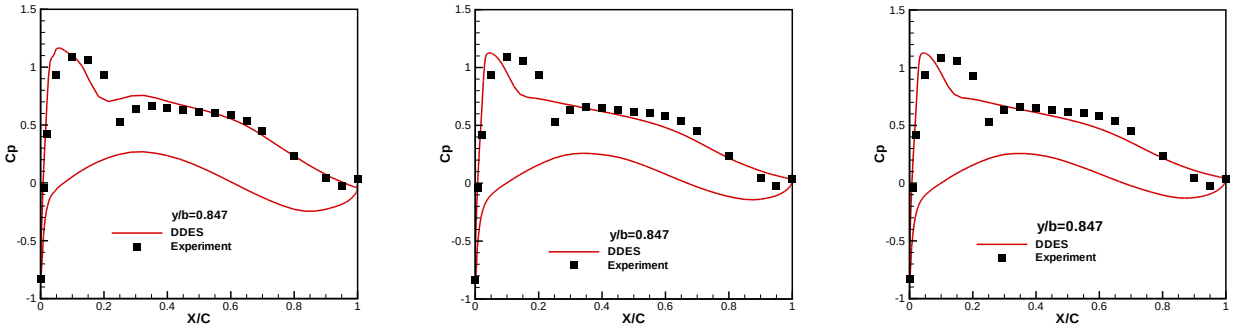

Figure 13: Wing pressure coefficient comparison using DDES at 0.847 semispan. Left: Coarse mesh; Middle: Medium mesh; Right: Fine mesh

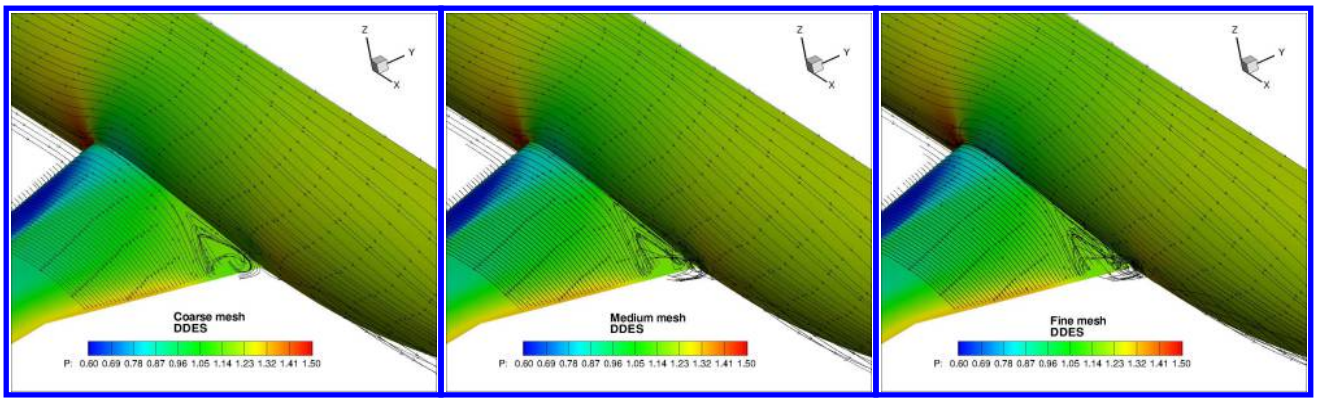

Figure 14: Surface pressure and streamline comparisons of different mesh sizes

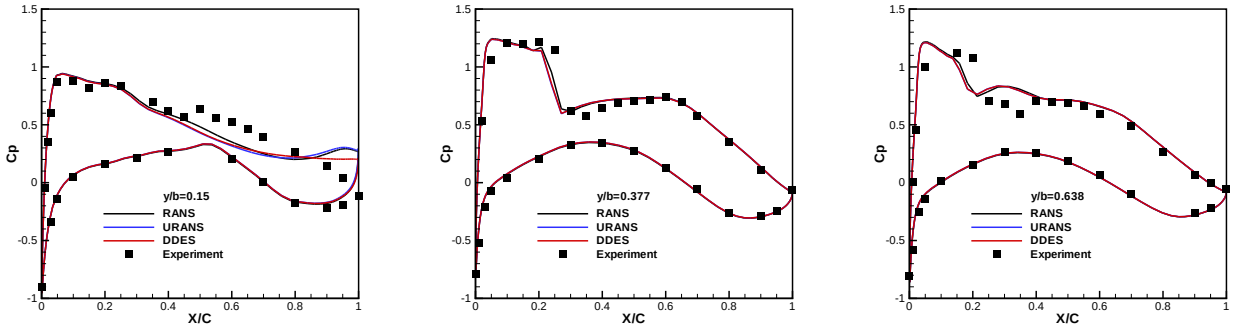

Figure 15: Pressure coefficient comparison at different wing span for AoA=0.49°, showing the effect of turbulence modeling

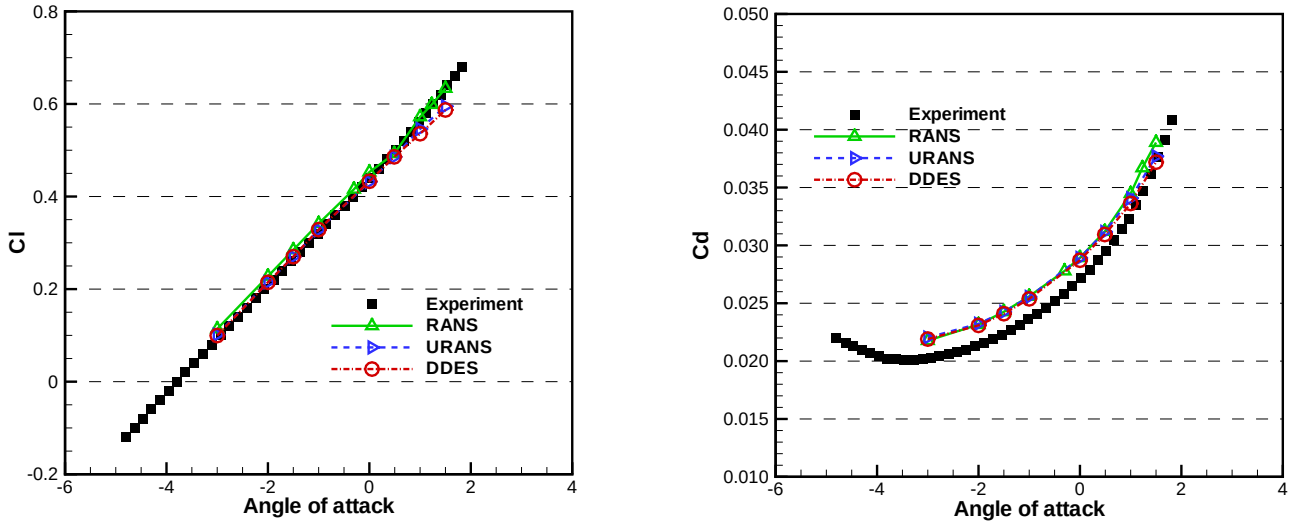

Figure 16: Lift curve (Left) and Drag curve (Right) of DLR-F6, showing the effect of turbulence modeling

References

[1] AIAA Drag Prediction Workshop, "http://aaac.larc.nasa.gov/tsab/cfdlarc/aiaa-dpw."

[2] D.W. Levy, T. Zickuhr, J.C. Vassberg, S. Agrawal, R.A. Wahls, S. Pirzadeh, M.J. Hemsch, "Summary of Data from the First AIAA CFD Drag Prediction Workshop." AIAA Paper 2002-0841, 2010.

[3] K. Laflin, O.P. Brodersen, M. Rakowitz, J.C. Vassberg, R.A. Wahls, J.H. Morrison, "Summary of Data from the SecondAIAA CFD Drag Prediction Workshop." AIAA Paper 2004-0555, 2004.

[4] J.C. Vassberg, E.N. Tinoco, M. Mani, O.P. Brodersen, B. Eisfeld, S. Crippa, R. A. Wahls, J.H. Morrison, T. Zickuhr, K.R. Laflin, D.J.Mavriplis, "Summary of the Third AIAA CFD Drag Prediction Workshop." AIAA Paper 2007-0260, 2007.

[5] J.C. Vassberg, E.N. Tinoco, M. Mani, B. Rider, T. Zickuhr, D.W. Levy, O.P. Brodersen, B. Eisfeld, S. Crippa, R. A. Wahls, J.H. Morrison, D.J.Mavriplis, M. Murayama, "Summary of the Fourth AIAA CFD Drag Prediction Workshop." AIAA Paper 2010-4547, 2010.

[6] P. Spalart, W.-H. Jou, M. Strelets, and S. Allmaras, "Comments on the Feasibility of LES for Wings, and on a Hybrid RANS/LES Approach." Advances in DNS/LES, 1st AFOSR Int. Conf. on DNS/LES, Greyden Press, Columbus, H., Aug. 4-8, 1997.

[7] P.R. Spalart, S. Deck, M. Shur, and K.D. Squires, "A New Version of Detached-Eddy Simulation, Resistant to Ambiguous Grid Densities," *Theoritical and Computational Fluid Dynamics*, vol. 20, pp. 181–195, 2006.

[8] X.D. Liu, S. Osher, T. Chan, "Weighted essentially non-oscillatory schemes," *J.Comput.Phys.*, vol. 115, pp. 200–212, 1994.

[9] G.-S. Jiang, C.-W. Shu, "Efficient implementation of weighted ENO schemes," *J.Comput.Phys.*, vol. 126, pp. 202–228, 1996.

[10] A.K. Henrick, T.D. Aslam, J.M. Powers, "Mapped weighted essentially non-oscillatory schemes:Achiving optimal order near critical points," *J.Comput.Phys.*, vol. 208, pp. 206–227, 2005.

[11] R. Borges, M. Carmona, B. Costa, W.S. Don, "An improved weighted essentially non-oscillatory scheme for hyperbolic conservation laws," *Journal of Computational Physics*, vol. 227, pp. 3191–3211, 2008.

[12] Z.J. Wang and R.F. Chen, "Optimized weighted essentially non-oscillatory schemes for linear waves with discontinuity," *J.Comput.Phys.*, vol. 174, pp. 381–404, 2001.

[13] Y.-Q. Shen, G.-C. Zha, "Improvement of weighted essentially non-oscillatory schemes near discontinuity." AIAA paper 2009-3655, 2009.

[14] Y.-Q. Shen, G.-C. Zha, B.-Y. Wang, "Improvement of stability and accuracy of implicit WENO scheme," *AIAA Journal*, vol. 47, pp. 331–344, 2009.

[15] D.S. Balsara, C.-W. Shu, "Monotonicity preserving weighted essentially non-oscillatory schemes with increasingly high order of accuracy," *J.Comput.Phys.*, vol. 160, pp. 405–452, 2000.

[16] M. P. Martin, E. M. Taylor, M. Wu, and V. G. Weirs, "A Bandwidth-Optimized WENO Scheme for the Direct Numerical Simulation of Compressible Turbulenc," *Journal of Computational Physics*, vol. 220, pp. 270–289, 2006.

[17] Y.-Q. Shen, G.-Z. Zha, X.-Y. Chen , "High order conservative differencing for viscous terms and the application to vortex-induced vibration flows," *Journal of Computational Physics*, vol. 228, pp. 8283–8300, 2009.

[18] Y.-Q. Shen, G.-Z. Zha, "Large eddy simulation using a new set of sixth order schemes for compressible viscous terms," *Journal of Computational Physics*, vol. 229, pp. 8296–8312, 2010.

[19] P. Spalart and S. Allmaras, "A One-equation Turbulence Model for Aerodynamic Flows." AIAA-92-0439, 1992.

[20] M. Shur, P. Spalart, M. Strelets, and A. Travin, "Detached-Eddy Simulation of an Airfoil at High Angle of Attack", 4th Int. Symp. Eng. Turb. Modelling and Measurements, Corsica." May 24-26, 1999.

[21] G. C. Zha, Y. Q. Shen, B. Y. Wang, "An improved low diffusion E-CUSP upwind scheme," *Computers & Fluids*, vol. 48, pp. 214–220, 2011.

[22] G.-C. Zha, Y.-Q. Shen, B.-Y. Wang, "Calculation of Transonic Flows Using WENO Method with a Low Diffusion E-CUSP Upwind Scheme." AIAA Paper 2008-0745, Jan 2008.

[23] P. Roe, "Approximate Riemann solvers, parameter vectors, and difference schemes," *Journal of Computational Physics*, vol. 43, pp. 357–372, 1981.

[24] J. R. Edwards, "A Low-Diffusion Flux-Splitting Scheme for Navier-Stokes Calculations," *Computer & Fluids*, vol. 6, pp. 635–659, 1997.

[25] B.Y. Wang, and G.C. Zha, "Comparison of a Low Diffusion E-CUSP and the Roe Scheme for RANS Calculation." AIAA Paper 2008-0596, 46th AIAA Aerospace Sciences Meeting and Exhibit, Jan. 7-10, 2008.

[26] A. Jameson, "Time Dependent Calculations Using Multigrid with Application to Unsteady Flows past Airfoils and Wings." AIAA Paper 91-1596, 1991.

[27] Y.-Q. Shen, B.-Y. Wang, G.-C. Zha, "Implicit WENO scheme and high order viscous formulas for compressible flows." AIAA-2007-4431, June 2007.